

## RESEARCH INTERNSHIP REPORT

December 2, 2019

---

# Lateral Dynamics Analysis and Controller Design of a Tilting Body Drone

---

Author: James Allen  
Supervisor: David Saussié



**POLYTECHNIQUE  
MONTRÉAL**

UNIVERSITÉ  
D'INGÉNIERIE

### Credit

Professor David Saussié  
Leandro Lustosa (PHD Thesis)  
Olivier Gougeon (Masters Thesis)

# Contents

<b>1</b>	<b>Introduction to Hybrid Aerial Vehicles</b>	<b>1</b>
<b>2</b>	<b>Theoretical Foundations</b>	<b>1</b>
2.1	MAVion Model . . . . .	1
2.2	Equilibrium Point Analysis and Linearisation . . . . .	2
2.3	State-Space Representation . . . . .	3
2.3.1	Reduced Quaternion Model: . . . . .	4
<b>3</b>	<b>Analysis of the Dynamic Model</b>	<b>4</b>
3.1	Actuator Saturation Limits . . . . .	4
3.2	Decoupling of Longitudinal and Lateral Dynamics . . . . .	4
3.3	Analysis of the Natural Dynamics . . . . .	6
<b>4</b>	<b>Lateral Motion Control</b>	<b>9</b>
4.1	Fundamental Properties . . . . .	9
4.2	Generic Lateral Control Architecture and Design . . . . .	9
4.3	MAVion Tilt-Body: Controllers . . . . .	11
4.3.1	Linear Quadratic Regulator . . . . .	11
<b>5</b>	<b>Conclusion</b>	<b>18</b>

## List of Figures

1	Atmos [2] . . . . .	1
2	WingtraOne [3] . . . . .	1
3	SkyTote [4] . . . . .	1
4	Detailed diagram of MAVion convertible drone . . . . .	2
5	Real life model of the MAVion . . . . .	2
6	Size of MAVion . . . . .	2
7	Actuator trim points for all velocities ranging from $v_{ne} = 0m/s$ to $v_{ne} = 30m/s$ . . . . .	3
8	Comprehensive Longitudinal Pole Map . . . . .	7
9	Comprehensive Lateral Pole Map . . . . .	8
10	RC Radio Architecture - Range of inputs to the MAVion from the drone operator . . . . .	9
11	Effect on $v_b$ and $\psi$ to a step response with no H matrix or integrator used . . . . .	12
12	Effect on $v_b$ and $\psi$ to a step response . . . . .	14
13	Effect on actuators $w$ and $\delta$ to a step response . . . . .	14
14	Effect on $v_b$ and $\psi$ to a step response . . . . .	17
15	Effect on actuators $w$ and $\delta$ to a step response . . . . .	17

## Nomenclature

$\Delta u$	Deviation in Input
$\Delta x$	Deviation in State
$\Delta y$	Deviation in Output
$\delta_1$	Left Elevon Deflection
$\delta_2$	Right Elevon Deflection
$\hat{b}_1$	Forward Axis
$\hat{b}_2$	Sideways Axis
$\hat{b}_3$	Up/Down Axis
$\mathcal{B}$	Body Frame
$\omega_1$	Left Propeller Angular Velocity
$\omega_2$	Right Propeller Angular Velocity
$\theta_e$	Equilibrium Pitch Angle
$A \in \mathbb{R}^{9 \times 9}$	State Matrix
$B \in \mathbb{R}^{9 \times 4}$	Input Matrix
$C \in \mathbb{R}^{9 \times 9}$	Output Matrix
$D \in \mathbb{R}^{9 \times 4}$	Feed-through Matrix
$m$	Number of Inputs
$n$	Number of States
$p$	Number of Outputs
$q \in \mathbb{R}^4$	Quaternion Representation
$Q \in \mathbb{R}^{n \times n}$	State Weighting Matrix
$R \in \mathbb{R}^{m \times m}$	Control Weighting Matrix
$u \in \mathbb{R}^4$	Input Matrix
$v_{ne}$	Equilibrium Forward Velocity
$w_e$	Equilibrium Propeller Angular Velocity
$x \in \mathbb{R}^{10}$	State Matrix
$y \in \mathbb{R}^9$	Output Matrix

# 1 Introduction to Hybrid Aerial Vehicles

Over the past few years, there has been significant research and development into Unmanned Aerial Vehicles (UAVs) and their impact on society. Despite most of these vehicles being either of a rotary wing quadcopter design or a fixed-wing plane like design, hybrid aerial vehicles (HAVs) have been increasingly gaining popularity. As the name suggests, these vehicles possess the ability to both hover when taking off and landing, and then tilt into plane-like flight when the velocity of the drone is increased. This unique ability allows the once slow quadcopter style drones to fly far greater distances at much higher speeds. A number of companies have been working on the development of these HAVs, with 3 common drones depicting the layout and design of these vehicles [1].



**Figure 1:** *Atmos* [2]



**Figure 2:** *WingtraOne* [3]



**Figure 3:** *SkyTote* [4]

As shown above, a common HAV design is the tail-sitting tilt-body drone. In addition to the obvious advantages such as distance and velocity, it also has other key factors that make this design worth investigating further. The first of these is the reduction in actuators in comparison to a regular 4-8 motor drone. With these HAVs often only requiring 2 motors and 2 actuators such as a servo to adjust the elevons, this means they are less prone to failure whilst flying. Another advantage is their slim body shape, with this allowing them to be far more easily transported and assembled. In addition to this, their impact on the environment is also reduced due to their weight. In the event of a crash, being significantly lighter means they may not cause such a large impact on the ground, trees, plants or animals that it may possibly land on [5].

Despite the positives of HAVs, these advantages such as reduced actuators, leads to challenges in both the stability and consistency of these drones. For this reason, it is important that further research is conducted regarding the stabilisation of the lateral motion of the common tail-sitting HAVs.

## 2 Theoretical Foundations

### 2.1 MAVion Model

In order to successfully analyse the lateral motion of the MAVion tilt body drone, it is important that all relevant actuators, motion directions and axis are presented. As seen in the figure below, the axis of orientation is typical to any standard aircraft, with the forward direction being represented as  $\hat{b}_1$ , lateral direction as  $\hat{b}_2$  and the vertical (up-down) direction as  $\hat{b}_3$ . In addition to the axis layout, the actuators and their relevant directions have also been included, with these presented in the list below:

- The MAVion is comprised of 2 motors, with their angular velocity being represented as  $w_1$  and  $w_2$ . These primarily affect the yawing moment by creating a differential of true angular velocities. It is also important to note that although the direction of motion for the motors is the same, the propellers rotate in opposite directions.
- The elevons are represented by  $\delta_1$  and  $\delta_2$ , with their deflections resulting in 2 possible moments. When both elevons are deflected in the same direction such that  $\delta_1 = \delta_2$ , this results in a pitching moment, whereas when  $\delta_1$  and  $\delta_2$  are deflected in opposite directions, this results in a rolling moment being generated.

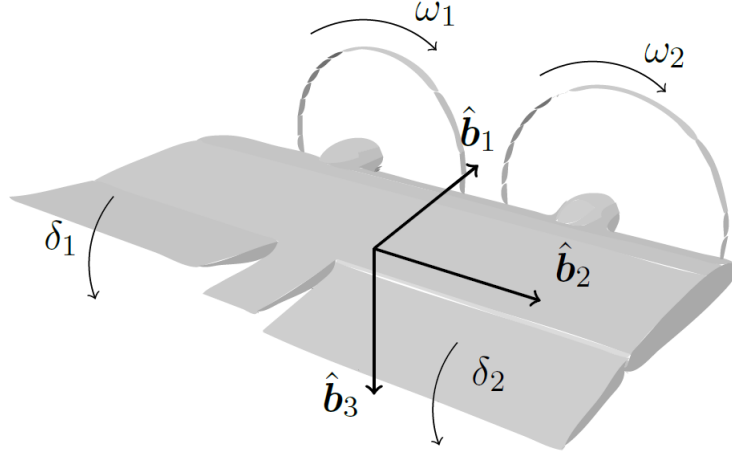


**Figure 4:** Detailed diagram of MAVion convertible drone

In addition to the rendered 3D model of the MAVion, a real life working drone has also been created as shown in the figure below. Although the actuators and directions of motion are now known from the model above, the use of this to-scale MAVion allows a greater understanding into reasonable response times and actuator saturation limits. As shown below, the MAVion is quite small ( $420mm \times 210mm$ ), providing insight into the fast and manoeuvrable nature of the drone. For this reason, it would be a reasonable assumption that adjustments in actuators should occur within the space of a few seconds, compared to a larger plane where a longer response time is acceptable.

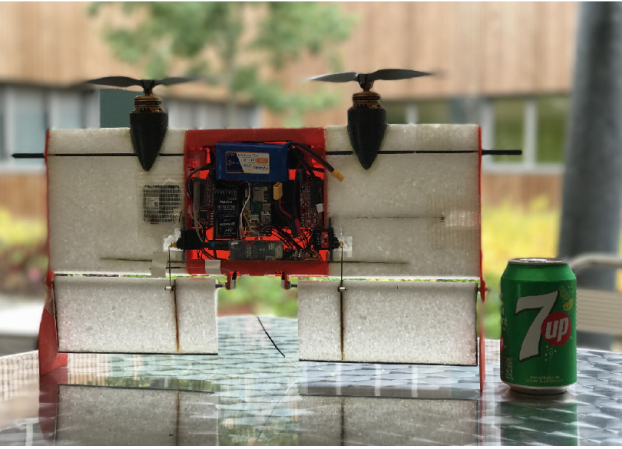


**Figure 5:** Real life model of the MAVion

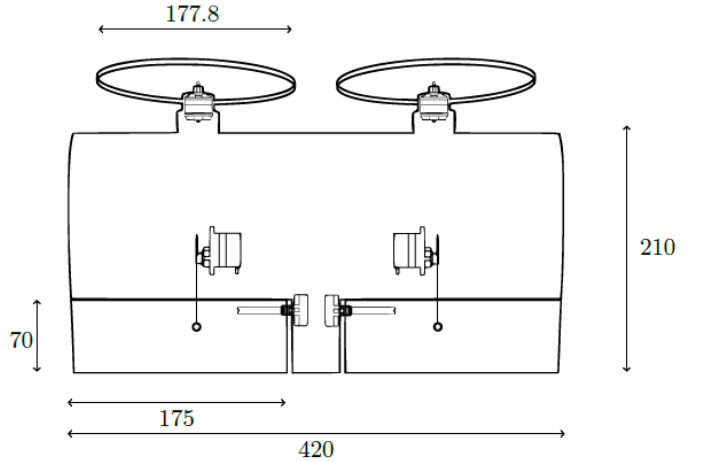


**Figure 6:** Size of MAVion

## 2.2 Equilibrium Point Analysis and Linearisation

In order to analyse the dynamics of the MAVion drone, the first and most important step is to balance the system for any velocity. This is often referred to as the trim or equilibrium conditions of the drone. In the case of the MAVion, this trim condition provides insight into the angular velocity of the motors, angular position and direction of each elevon, along with the resulting flight characteristics due to these actuator changes. These include the forward, lateral and vertical velocity ( $v_b$ ), forward, lateral and vertical angular velocity ( $w_b$ ) and the Quaternion angles at the equilibrium point. A detailed plot of this can be seen below, with the first graph depicting the angular velocity of the motors ( $w_e$ ) and the second showing the angular position of the elevons ( $\delta_e$ ).

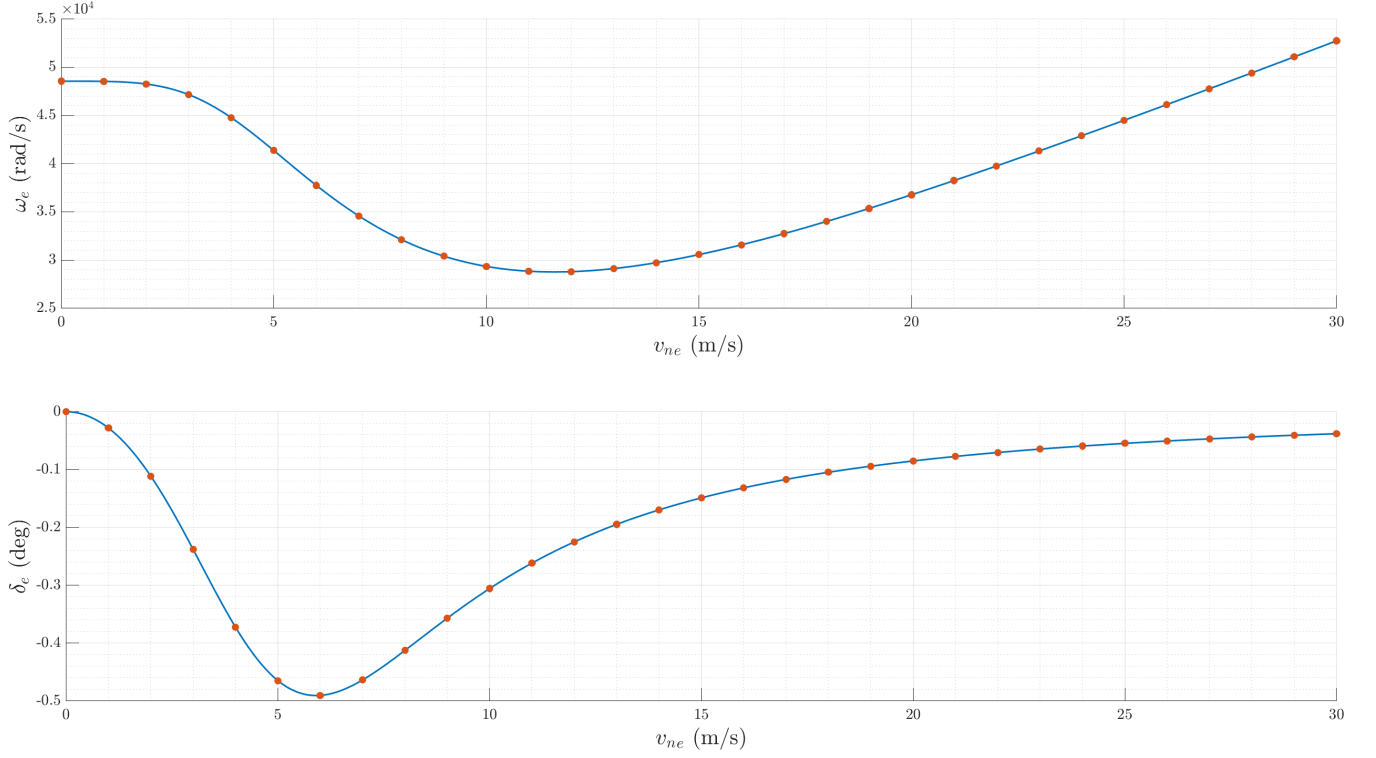


**Figure 7:** Actuator trim points for all velocities ranging from  $v_{ne} = 0\text{m/s}$  to  $v_{ne} = 30\text{m/s}$

### 2.3 State-Space Representation

A common method for representing the properties of a dynamical system is through the use of the State-Space model. This representation uses a set of state variables to accurately and effectively determine the outputs of the system given the predefined inputs and states. In the standard mathematical form, the state-space model is defined as N first order ordinary differential equations (ODEs) as follows:

$$\dot{x} = f(x, u) \quad (1)$$

Where the states and inputs from this form can be represented as the following set of equations when considering the full 6DOF dynamical model:

$$\begin{aligned} x &= [v_b \ w_b \ q]^T \\ u &= [w_1 \ w_2 \ \delta_1 \ \delta_2]^T \end{aligned} \quad (2)$$

After linearisation of the system as previously discussed, the state and input vectors are as follows:

$$\begin{aligned} \Delta x &= [\Delta v_b \ \Delta w_b \ \psi]^T \\ \Delta u &= [\Delta w_1 \ \Delta w_2 \ \Delta \delta_1 \ \Delta \delta_2]^T \end{aligned} \quad (3)$$

The final state-space equations can be represented in the following form:

$$\begin{aligned} \Delta \dot{\mathbf{x}} &= \mathbf{A} \Delta \mathbf{x} + \mathbf{B} \Delta \mathbf{u} \\ \Delta \mathbf{y} &= \mathbf{C} \Delta \mathbf{x} + \mathbf{D} \Delta \mathbf{u} \end{aligned} \quad (4)$$

And when D is set to 0, the output equation ends up in the final form:

$$\Delta \mathbf{y} = \mathbf{C} \Delta \mathbf{x} \quad (5)$$

### 2.3.1 Reduced Quaternion Model:

Although there are 10 states of the system ( $v_b$ ,  $w_b$  and  $q$ ), it can be seen that there are only 9 outputs. If the system retains all states to allow it to have 10 poles, this makes the linear analysis complex seeing as it is a non-minimal representation of the angular position. After linearising the 10 ODEs, the order of the system drops by 1 rank due to the quaternions being linked to the constraint equation below.

$$q_0 = \pm\sqrt{1 - q_1^2 - q_2^2 - q_3^2} \quad (6)$$

## 3 Analysis of the Dynamic Model

### 3.1 Actuator Saturation Limits

In order to successfully analyse the MAVion dynamic model, it is firstly important that the saturation limits of all of the actuators and flight conditions are addressed. Arguably the most essential limit of the MAVion is the range of forward flight velocities ( $v_{ne}$ ). In the model being analysed, the drone has a minimum velocity of  $v_{ne} = 0m/s$  and a maximum velocity of  $v_{ne} = 30m/s$ . At this maximum forward velocity, the propellers are required to operate at a speed of  $w_{sat} = 920rad/s$ . Along with this, the elevons also have a saturation value, with the maximum deflection being  $\delta_{sat} = \pm 27deg$ . The reason this is a key factor is due to each of the actuators having a physical limit that could either damage the system or simply halt the required operation from occurring. These saturation limits have been summarised in the table below.

Actuator/Condition	Physical Limit
$v_{ne}$	[0,30] m/s
$w_{sat}$	[0,920] rad/s
$\delta_{sat}$	[-27,27] deg

With the limitations of the MAVion addressed, the dynamics of the model can now be analysed in detail. This ensures that no damage will occur simply due to a saturation value being reached.

### 3.2 Decoupling of Longitudinal and Lateral Dynamics

A useful way of analysing the dynamics of a 6DOF model is to separate these into the longitudinal and lateral components. Although it is possible to decouple the dynamics of a regular airplane, a detailed analysis will be conducted in order to determine whether decoupling of the MAVion model is possible. As previously detailed, the system is made up of 9 poles, with 4 of these being the longitudinal states, and 5 as the lateral states. Recall these states and inputs as follows:

$$\begin{aligned} \Delta x &= [\Delta v_b \ \Delta w_b \ \psi]^T \\ \Delta u &= [\Delta w_1 \ \Delta w_2 \ \Delta \delta_1 \ \Delta \delta_2]^T \end{aligned} \quad (7)$$

With the states from above being expanded into the following form, this allows decoupling to be possible:

$$\begin{aligned} \Delta v_b &= [\Delta u_b \ \Delta v_b \ \Delta w_b] \\ \Delta w_b &= [\Delta p \ \Delta q \ \Delta r] \\ \psi &= [\Delta \phi \ \Delta \theta \ \Delta \psi] \end{aligned} \quad (8)$$

And hence the expanded state space matrix can now be represented:

$$\Delta x = [\Delta u_b \ \Delta v_b \ \Delta w_b \ \Delta p \ \Delta q \ \Delta r \ \Delta \phi \ \Delta \theta \ \Delta \psi]^T \quad (9)$$

From the above states, it is possible to separate these into the Longitudinal states and inputs:

$$\begin{aligned} \Delta x &= [\Delta u_b \ \Delta w_b \ \Delta q \ \Delta \theta]^T \\ \Delta u &= [\Delta w_1 \ \Delta \delta_1]^T \text{ or, } \Delta u = [\Delta w_2 \ \Delta \delta_2]^T \end{aligned} \quad (10)$$

And similarly into the Lateral states and inputs:

$$\begin{aligned}\Delta x &= [\Delta v_b \ \Delta p \ \Delta r \ \Delta \phi \ \Delta \psi]^T \\ \Delta u &= [\Delta w_1 \ \Delta \delta_1]^T \text{ or, } \Delta u = [\Delta w_2 \ \Delta \delta_2]^T\end{aligned}\tag{11}$$

After the separation of these states and inputs into their respective modes (longitudinal or lateral), it is then possible to analyse the model to determine whether decoupling is possible for any forward velocity of the MAVion. Before conducting this research, a hypothesis was presented to predict the outcome of this analysis. This hypothesis is as follows:

**Hypothesis 1 (H1):** *As the drone begins flight as a typically unstable quadcopter and gradually tilts into stable plane like flight, it is likely that decoupling will be possible when the drone is flying at high velocities as this closely replicates that of a plane. However, at lower velocities when the MAVion is in a tilt configuration of flight, it is predicted that decoupling will not be feasible.*

Interestingly, after significant analysis of the MAVion following the equations presented in (11), it was proven that decoupling was possible for any forward velocity, hence rendering the closing statement of hypothesis (1) as invalid. In order to determine the accuracy of this hypothesis, a detailed comparison between the poles from the full dynamic model and the decoupled Lateral system was undertaken. A table below has been presented which lists a number of key velocities analysed and their respective poles. In order for the decoupling of the system to be possible, these poles should very closely match.

Velocity (m/s)	6DOF Lateral Poles	Decoupled Lateral Poles	Match: Y/N?
30	$-1.98 \times 10^1$ $-8.10 \times 10^0$ $-2.21 \times 10^0$ $4.57 \times 10^{-4}$ $3.15 \times 10^{-15}$	$-1.98 \times 10^1$ $-8.10 \times 10^0$ $-2.21 \times 10^0$ $4.57 \times 10^{-4}$ $2.20 \times 10^{-14}$	Y
20	$-1.32 \times 10^1$ $-5.44 \times 10^0$ $-1.47 \times 10^0$ $1.68 \times 10^{-3}$ $5.24 \times 10^{-16}$	$-1.32 \times 10^1$ $-5.44 \times 10^0$ $-1.47 \times 10^0$ $1.68 \times 10^{-3}$ $-1.80 \times 10^{-14}$	Y
10	$-6.32 \times 10^0$ $-3.05 \times 10^0$ $-7.10 \times 10^{-1}$ $2.95 \times 10^{-2}$ $-1.42 \times 10^{-16}$	$-6.32 \times 10^0$ $-3.05 \times 10^0$ $-7.10 \times 10^{-1}$ $2.95 \times 10^{-2}$ $4.99 \times 10^{-15}$	Y
5	$-2.90 \times 10^0$ $-1.65 \times 10^0$ $-8.02 \times 10^{-1}$ $3.19 \times 10^{-1}$ $1.73 \times 10^{-16}$	$-2.90 \times 10^0$ $-1.65 \times 10^0$ $-8.02 \times 10^{-1}$ $3.19 \times 10^{-1}$ $2.90 \times 10^{-16}$	Y
4	$-2.46 \times 10^0$ $-9.88 \times 10^{-1} \pm j4.03 \times 10^{-1}$ $4.10 \times 10^{-1}$ $2.36 \times 10^{-16}$	$-2.46 \times 10^0$ $-9.88 \times 10^{-1} \pm j4.03 \times 10^{-1}$ $4.10 \times 10^{-1}$ $-1.81 \times 10^{-16}$	Y
1	$4.33 \times 10^{-1}$ $-3.88 \times 10^{-1} \pm j4.53 \times 10^{-1}$ $-6.61 \times 10^{-1}$ $-1.36 \times 10^{-17}$	$4.33 \times 10^{-1}$ $-3.88 \times 10^{-1} \pm j4.53 \times 10^{-1}$ $-6.61 \times 10^{-1}$ $1.64 \times 10^{-17}$	Y

**Table 1:** *Decoupling of Lateral Dynamics*

The results above confirm that decoupling of the Lateral dynamics can be successfully applied on the MAVion drone. Although the smallest real pole from each set of velocities does not perfectly match, it



should be noted that these are extremely small numbers all sitting very close to zero. For this reason, this level of error is of an acceptable nature and can therefore be disregarded and concluded as a match.

As previously suggested in hypothesis (1), at faster velocities when the MAVion is in plane like flight, the poles all appear to follow a similar trend and clearly match the 6DOF full dynamic model. Although at lower velocities the poles still appear to match, it can be noted that the system develops a complex conjugate pair. Although this will change the flying qualities of the drone, decoupling is still possible seeing as both the 6DOF poles and decoupled lateral poles simultaneously experience this change.

### 3.3 Analysis of the Natural Dynamics

As the dynamics of the MAVion can be successfully decoupled for any of the possible flight velocities ( $0m/s \leq v_{ne} \leq 30m/s$ ), a detailed analysis will now be presented. This analysis involves inspecting the poles of the longitudinal and lateral transfer functions, to therefore determine the modes of the system. If the transfer function is shown to depict longitudinal dynamics, the only poles/modes remaining will be the short period and phugoid modes. Similarly, if the transfer function corresponds to the lateral dynamics, the only modes present will be the dutch roll, spiral and roll subsidence modes. This provides insight into the flying qualities of the drone, and how this tilt-body may act at certain velocities. In order to analyse the poles of the system, the fundamental theory behind how these were found will be detailed.

To find the poles of the model, the time-domain state space model should be converted into the s-domain using a Laplace transform as follows:

$$\begin{aligned} X(S) &= \mathcal{L}\{\dot{x}\} \\ X(S) &= (sI - A)^{-1}BU(s) \end{aligned}$$

And similarly,

$$\begin{aligned} Y(S) &= \mathcal{L}\{y\} \\ Y(S) &= CX(s) + DU(s) \end{aligned}$$

And hence,

$$G(S) = C(sI - A)^{-1}B + D$$

Using these transfer functions, the poles can be simply found by computing the eigenvalues of A:

$$\lambda_{k,l} = (sI - A)^{-1}$$

And subsequently resulting in the following form:

$$\lambda_{jk,l} = \sigma_{jk,l} \pm jw_{jk,l}$$

Where  $\sigma_{jk,l}$  is the real component and  $jw_{jk,l}$  is the imaginary component of the poles.

#### Analysis of Longitudinal Poles

After decoupling the longitudinal dynamics and finding the respective transfer functions relating both inputs to each of the 4 outputs, 2 complex conjugate poles were found for each transfer function. The first of these pairs is a fast pole associated with the short period mode, and the second complex conjugate pair is a slow pole related to the phugoid mode. In addition to this, it can be concluded that 2 of these poles are associated with the dynamics of the actuators. As previously detailed, due to the decoupling of the longitudinal dynamics, the single dimension reduction simplifies the actuators to the form:  $w = -w_1 = w_2$  and  $\delta = \delta_1 = \delta_2$ . This is the reason why there are only 2 poles related to the actuators despite the MAVion having 4 actuators present.

To further analyse the longitudinal dynamics and determine which complex conjugate pair relates to the phugoid and short period mode, an arbitrary forward velocity of  $20m/s$  was selected. After finding the roots of the transfer functions for this velocity, the following pairs were found:

$$Pole\ 1 = -9.665 \pm j27.386$$

$$Pole\ 2 = -0.259 \pm j0.586$$

Using these poles, each of the modes can be determined by finding the natural frequency, damping ratio and period. These were found using the following equations:

$$w_n = \sqrt{\sigma^2 + w^2};$$

$$\zeta = \frac{\sigma}{w_n}$$

$$T = \frac{2\pi}{w_n\sqrt{1 - w_n^2}}$$

With the subsequent results as follows:

$$Pole\ 1\ Characteristics : w_n = 29.04rad/s, \zeta = 0.333, T = 0.229s$$

$$Pole\ 2\ Characteristics : w_n = 0.641rad/s, \zeta = 0.405, T = 10.716s$$

From the results above, it is clear that the first complex conjugate pair corresponds to the short period mode and that the second pair corresponds to the phugoid mode seeing as they are separated by more than an order of magnitude. With the modes separated, it is then possible to represent these Longitudinal modes in a pole map. This displays both the phugoid and short period mode as shown below:

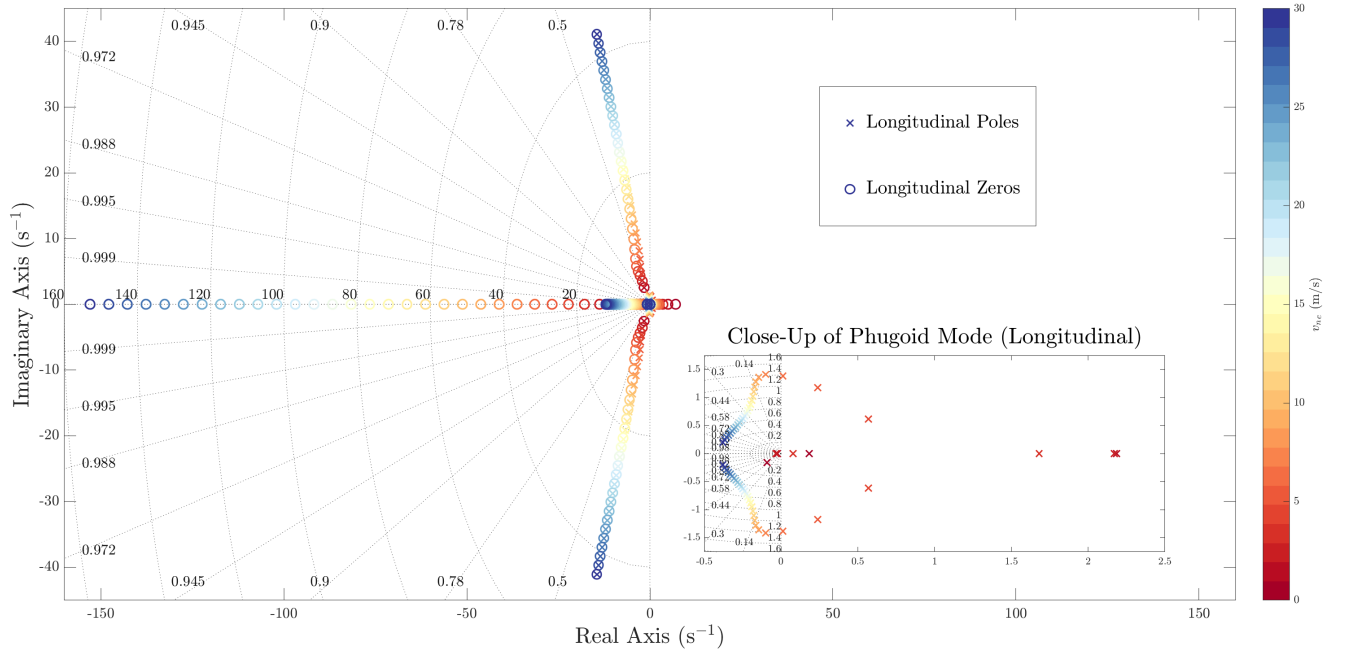


**Figure 8:** *Comprehensive Longitudinal Pole Map*

### Analysis of Lateral Poles

Although the longitudinal modes of the system appear to follow a reasonably standard form, consisting of a phugoid and short period mode, the lateral dynamics are more unique than a regular airplane. Typically, the lateral modes present on a plane are purely the dutch roll, spiral and roll subsidence mode. After analysing the poles of the decoupled dynamics, it is clear that for all velocities above  $4m/s$ , there are no complex conjugate pairs. With the dutch roll mode usually being easily recognisable from this pair of poles, it is clear that that this difference is likely due to the tilt-body flight

characteristics of the drone.

After further analysis of the poles, it is clear that the largest pole from each set of lateral transfer functions is the roll subsidence mode of the MAVion. Similarly, it can be concluded that the very small pole almost sitting on zero is related to the yaw state from the lateral matrix. The other small real pole is therefore associated with the spiral mode, leaving 2 real poles remaining. Although the dutch roll mode is typically a complex conjugate pair, allowing a visual inspection to simply reveal this mode, further analysis showed that these final 2 real poles are related to the dutch roll mode.

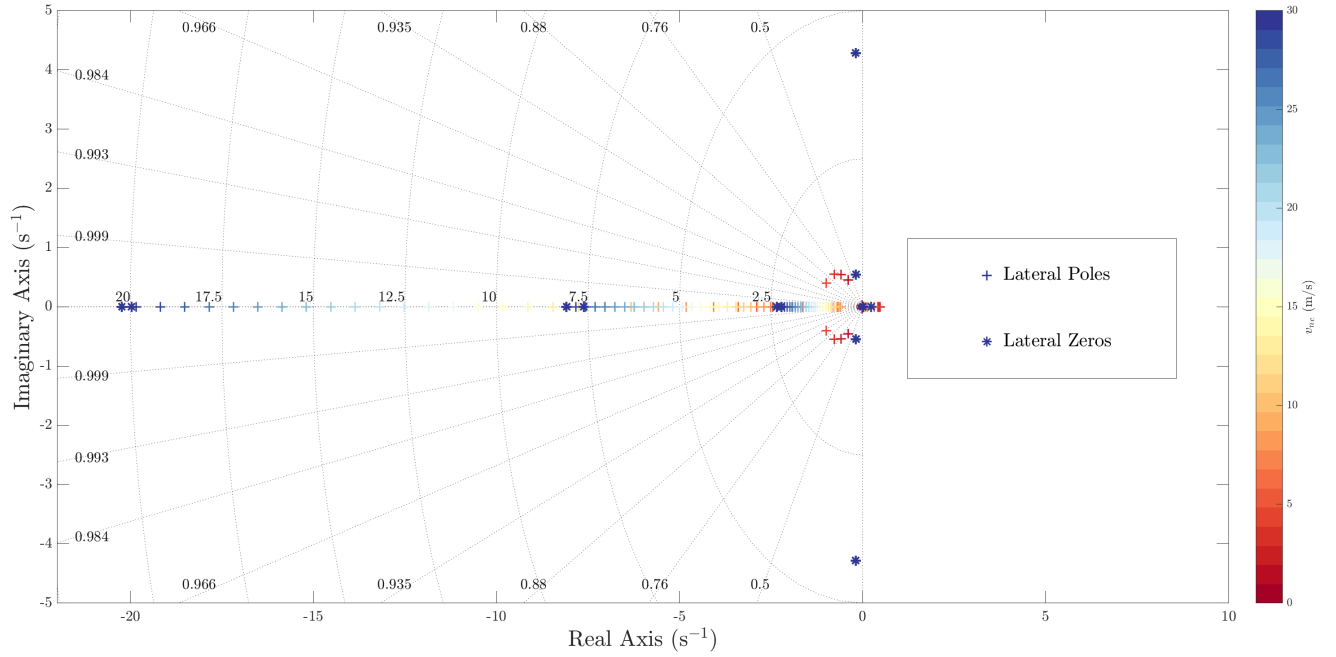


**Figure 9:** *Comprehensive Lateral Pole Map*

## 4 Lateral Motion Control

### 4.1 Fundamental Properties

After the detailed dynamical analysis of the MAVion drone, the control system for the lateral motion was of high importance. Before designing this controller, the following should be recalled:

The lateral system is composed of the following states:

$$\Delta x = [v_b \ p \ r \ \phi \ \psi]^T \quad (12)$$

And,

$v_b = \text{Lateral Velocity},$

$p = \text{Roll Rate},$

$r = \text{Yaw Rate},$

$\phi = \text{Roll},$

$\psi = \text{Yaw}$

In addition to this, another important consideration before designing the lateral autopilot was the RC radio architecture. From the diagram below, it can be seen that the pilot must fly the drone through adjustments of  $V_z$ ,  $V_y$ ,  $V_x$  and  $\dot{\psi}$ . As the control system being developed will required a desired input from the pilot, this is an important factor to keep in mind.

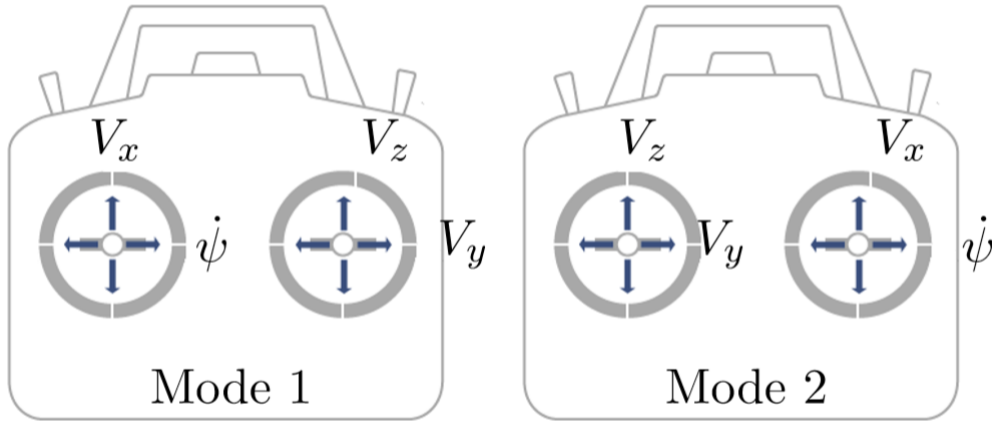


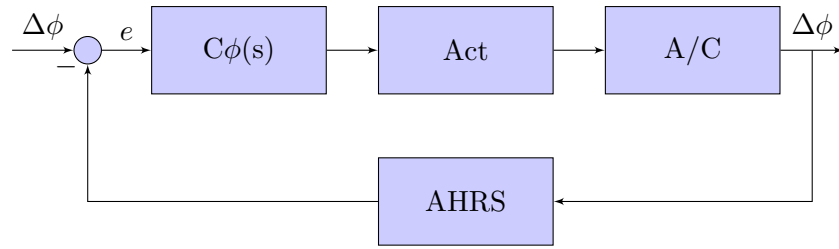
**Figure 10:** RC Radio Architecture - Range of inputs to the MAVion from the drone operator

### 4.2 Generic Lateral Control Architecture and Design

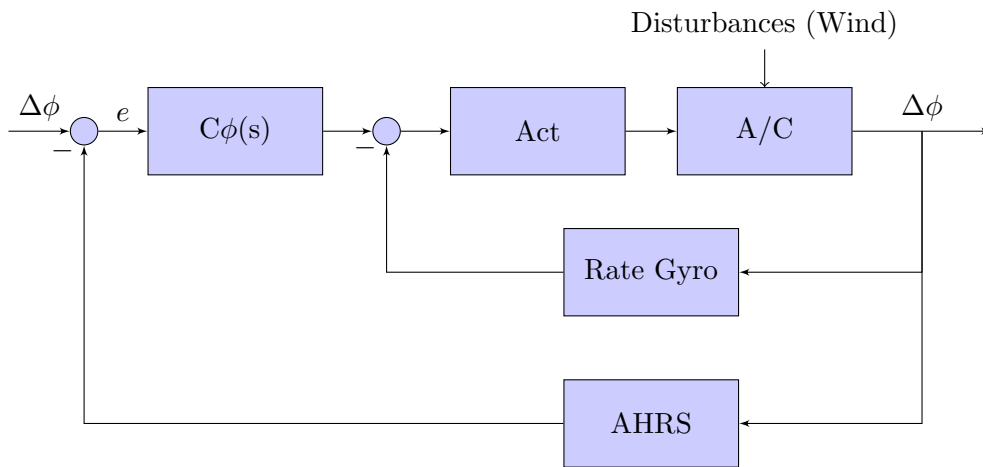
The first element in the control system design is to consider the lateral controls related to the RC radio being used. As previously depicted in Figure 3, the operator is required to fly the MAVion purely through adjustments of  $V_z$ ,  $V_y$ ,  $V_x$  and  $\dot{\psi}$ . Using the longitudinal and lateral decomposition techniques drawn upon in section 2.4, it can be determined that  $V_z$  and  $V_x$  are related to the vertical (up-down) and forward longitudinal velocities, and that  $V_y$  and  $\dot{\psi}$  are related to the lateral velocity and yaw rate, respectively. In addition to this, it is known that  $p$ ,  $r$  and  $\phi$  are also directly related to the lateral dynamics of the drone. Therefore, when designing the lateral control system, both the required dynamics and operator's needs will be closely followed.

In order to begin designing the lateral control system for the MAVion, the roll and yaw attitude commands will be analysed as separate subsystems to gain a better understanding of the autopilot requirements. The roll-angle control system will be designed first, with this being required in order to

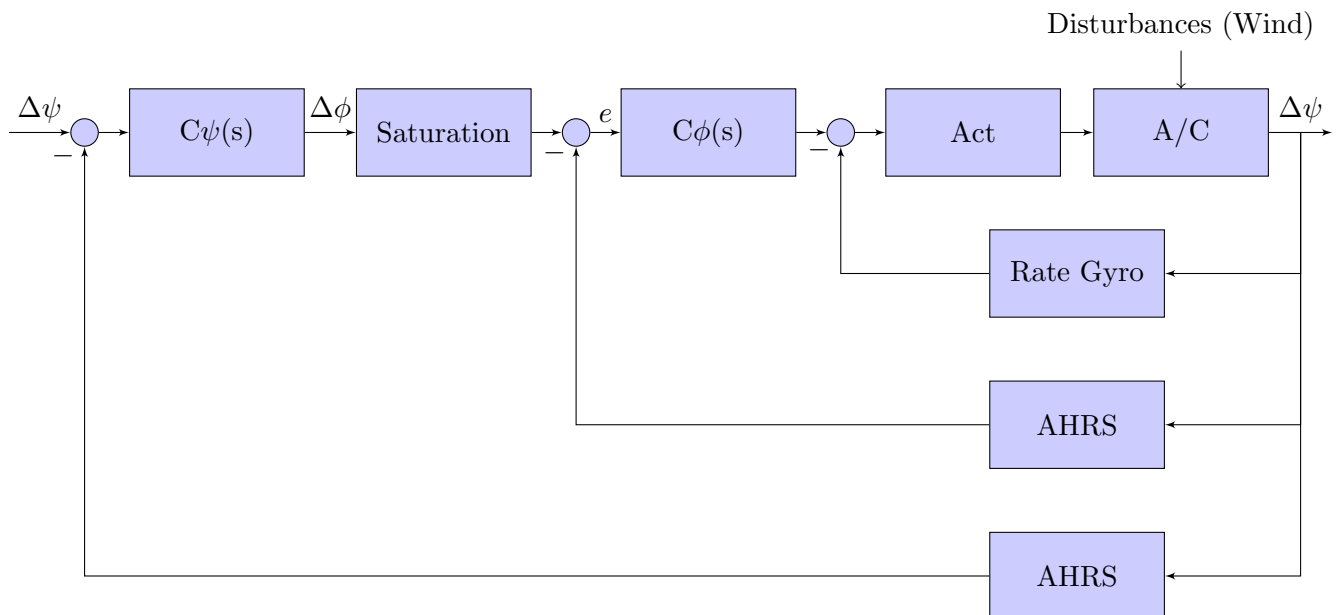
maintain the desired roll angle set by the pilot. In a very basic form, the following closed loop control system could be used to purely stabilise the roll of the aircraft. This can be seen in the figure below:



Building upon the above control system, additional features can be included to enhance the performance. For instance, a Stability Augmentation System (SAS) has been added into the previous control loop to improve the functionality of the system. This is used to provide inner loop rate damping for the autopilot. A control loop has been displayed below with this inclusion present:



With the roll-angle hold autopilot complete, the yaw control system can now be designed as this is also an important consideration for banked turns. When developing the control system for the lateral motion, the yaw can be related to the roll due to the strong coupling relationship present during flight. Therefore, when considering the control system for the lateral motion, it was of high importance that this roll-yaw coupling was considered. This autopilot can be seen below, and depicts a yaw-heading autopilot with an inner loop roll-angle autopilot and SAS.



### 4.3 MAVion Tilt-Body: Controllers

As the lateral control architecture has now been designed and analysed, a specific type of controller must be chosen to suit the needs of the MAVion. With the drone having a tilt body design, this yields most linear control techniques ineffective, meaning that non-linear controllers should instead be analysed. One of the most common controllers is the Linear Quadratic Regulator (LQR). This form of controller is one of the most common methods as it provides optimally controlled gains to successfully allow the closed loop system to be stable, whilst also performing at a high standard.

#### 4.3.1 Linear Quadratic Regulator

In order to create an LQR controller and hence find the optimal gain matrix of the system, the first step is to find the minimised cost function

$$J := \frac{1}{2} \int_0^\infty (\Delta x^T Q \Delta x + \Delta u^T R \Delta u) dt \quad (13)$$

Where  $R \in \mathbb{R}^{m \times m}$  and  $Q \in \mathbb{R}^{n \times n}$ , with these relating to the control and state weighting matrix, respectively. Similarly,  $\Delta x$  and  $\Delta u$  are the deviations in state and input as previously drawn upon in the following equation:

$$\dot{x} = A\Delta x + B\Delta u \quad (14)$$

In order to create a closed loop system and hence stabilise the lateral motion of the MAVion, the following feedback control law is used. This minimises the overall value of the cost:

$$\Delta u = -K\Delta x \quad (15)$$

After substituting this into equation 15, the following closed loop system is achieved:

$$\dot{x} = (A - BK)\Delta x \quad (16)$$

Where K can be found using the following equation:

$$K = R^{-1}B^T P \quad (17)$$

And where P is the solution to the Algebraic Riccati Equation (ARE):

$$A_i^T P_i + P_i A_i - P_i B_i B_i^T P_i + Q_i = 0 \quad (18)$$

#### Preliminary LQR Results:

With a basic LQR controller designed, this can now be implemented in MATLAB for a forward velocity of  $v_{ne} = 30m/s$ . After selecting appropriate gains to achieve a fast settling time, minimal peak response and fast rise time, the following plot was generated. As shown below, the lateral control system appears to work as expected except for the steady state values achieved.

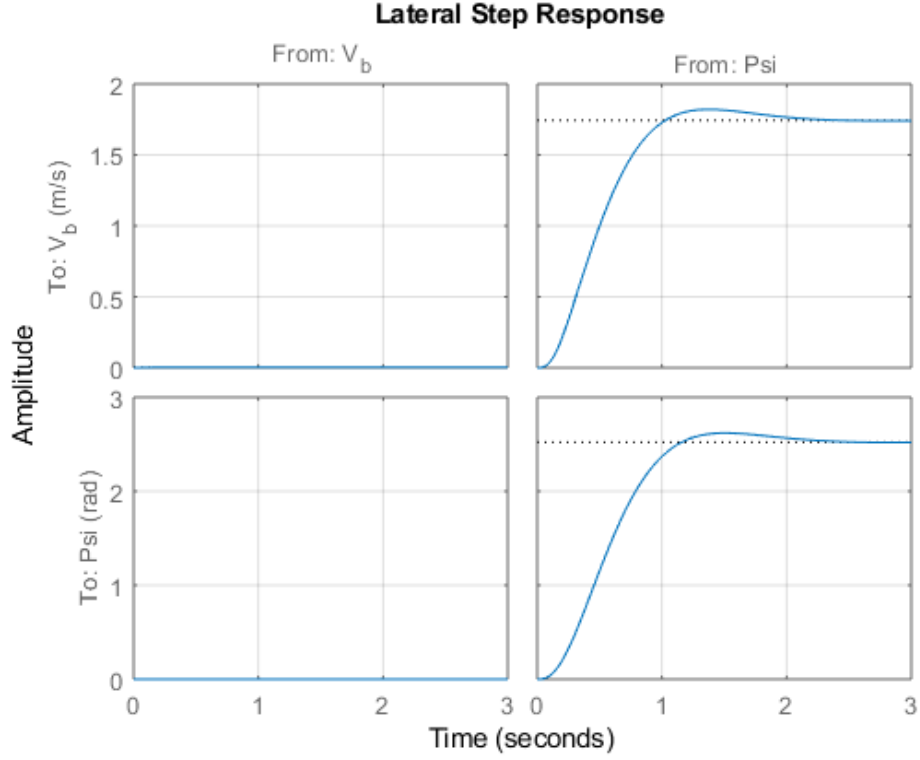


**Figure 11:** *Effect on  $v_b$  and  $\psi$  to a step response with no  $H$  matrix or integrator used*

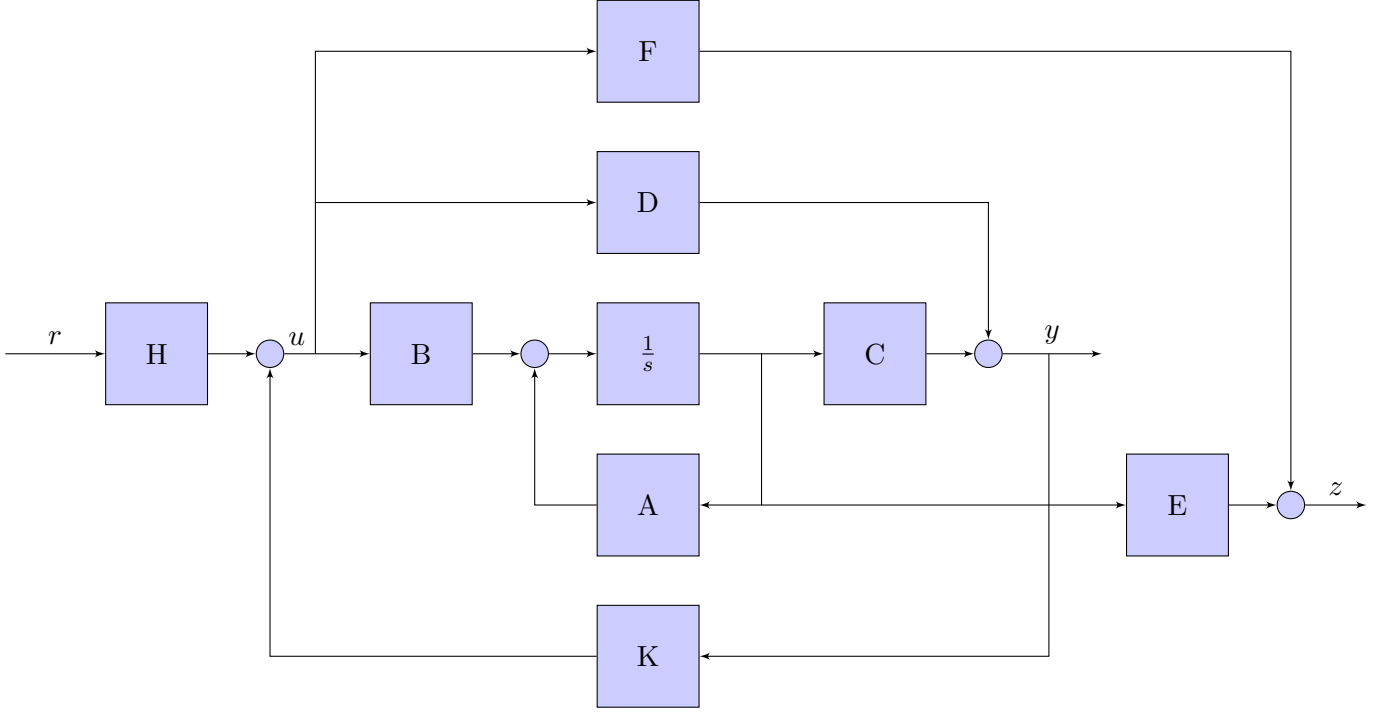
In order to design an effective LQR controller and hence fix this steady state issue, a solution should be implemented that allows the response to meet the desired steady state behaviour. This can be achieved using a number of possible methods, with 2 of these being detailed below. In addition to this, a detailed analysis has also been presented, allowing the most effective method to be selected.

#### **H Matrix Method:**

In order to develop an H matrix capable of producing the desired steady state behaviours, the system must first be analysed in detail. Although it is possible to simply control all outputs using this method, it also allows for specific outputs to be controlled. To achieve this effect, the following state space representations should be recalled and defined.

$$\begin{aligned} \dot{x} &= Ax + Bu \\ y &= Cx + Du \\ z &= Ex + Fu \end{aligned} \tag{19}$$

In the above state space equations, it can be noted that an additional equation is also presented. This represents the set of outputs that need to be controlled, with  $z \in \mathbb{R}^m$ . With the RC radio receiving commands from  $v_b$  (lateral velocity) and  $\dot{\psi}$  (yaw rate), these are the only outputs that should be controlled. In order to further describe this method, a diagram has been presented below to depict its functionality.



As seen above, the control law is simply the error at the  $u$  output. This results in the following equation:

$$u = -Ky + Hr \quad (20)$$

And to further expand equation 20, the output equation  $y$ , previously presented in equation 19 can be substituted in:

$$u = -K(Cx + Du) + Hr \quad (21)$$

Through the substitution of equation 21 into equations 19, the following expansion can be made:

$$\begin{aligned} \dot{x} &= Ax + B(-K(Cx + Du) + Hr) \\ y &= Cx + D(-K(Cx + Du) + Hr) \\ z &= Ex + F(-K(Cx + Du) + Hr) \end{aligned} \quad (22)$$

Which can then be simplified to the following form:

$$\begin{aligned} \dot{x} &= (A - B(I + KD)^{-1}KC)x + B(I + KD)^{-1}Hr \\ z &= (E - F(I + KD)^{-1}KC)x + F(I + KD)^{-1}Hr \end{aligned} \quad (23)$$

And when considering  $C = I$  and  $D = 0$ , the final set of equations is obtained:

$$\begin{aligned} \dot{x} &= (A - BK)x + B Hr \\ z &= (E - FK)x + F Hr \end{aligned} \quad (24)$$

With the closed loop state space system now developed, it is possible to analyse the effect of including the  $H$  matrix in the system. This is possible by analysing the effect of a step response on the system. It can be seen in the figure below that all plots either converge to 0 or 1, providing evidence that the  $H$  matrix is working as expected. In addition to this, it can be seen that the settling time and peak response is of an acceptable nature for a small scale drone such as the MAVion.



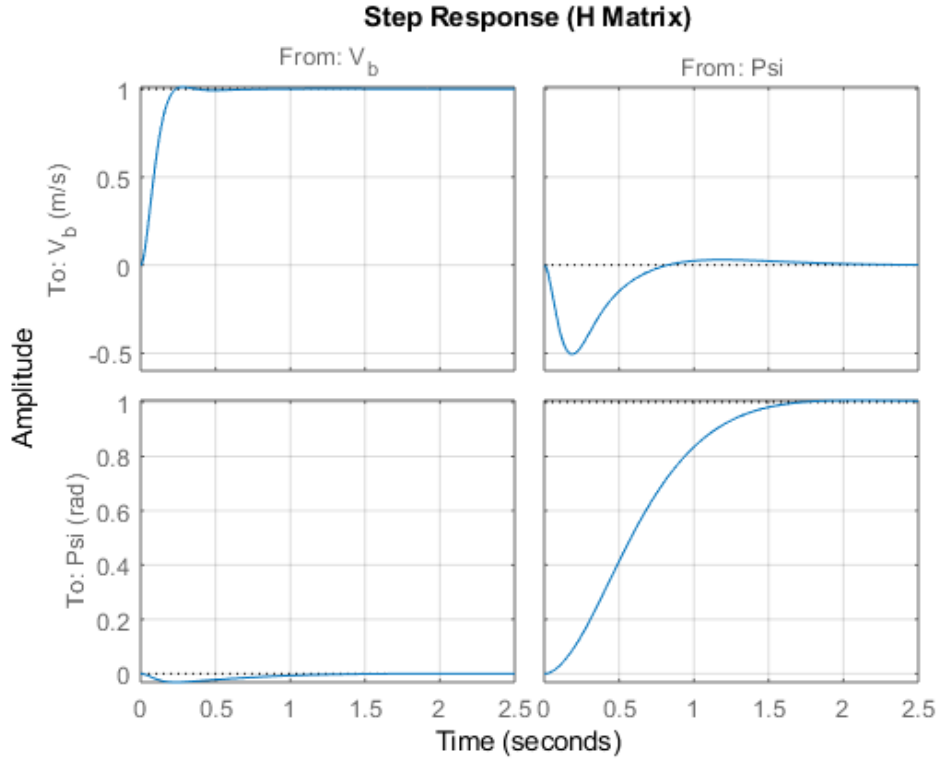


**Figure 12:** *Effect on  $v_b$  and  $\psi$  to a step response*

Along with this, it is also important to consider the saturation limits of the actuators ( $w$  and  $\delta$ ), as previously discussed. If these are not considered, it is possible that the tuned controller may not physically work on the model due to certain actuators reaching their maximum limits. The plot below shows the actuator movements when the forward velocity is set to  $v_{ne} = 30m/s$ .

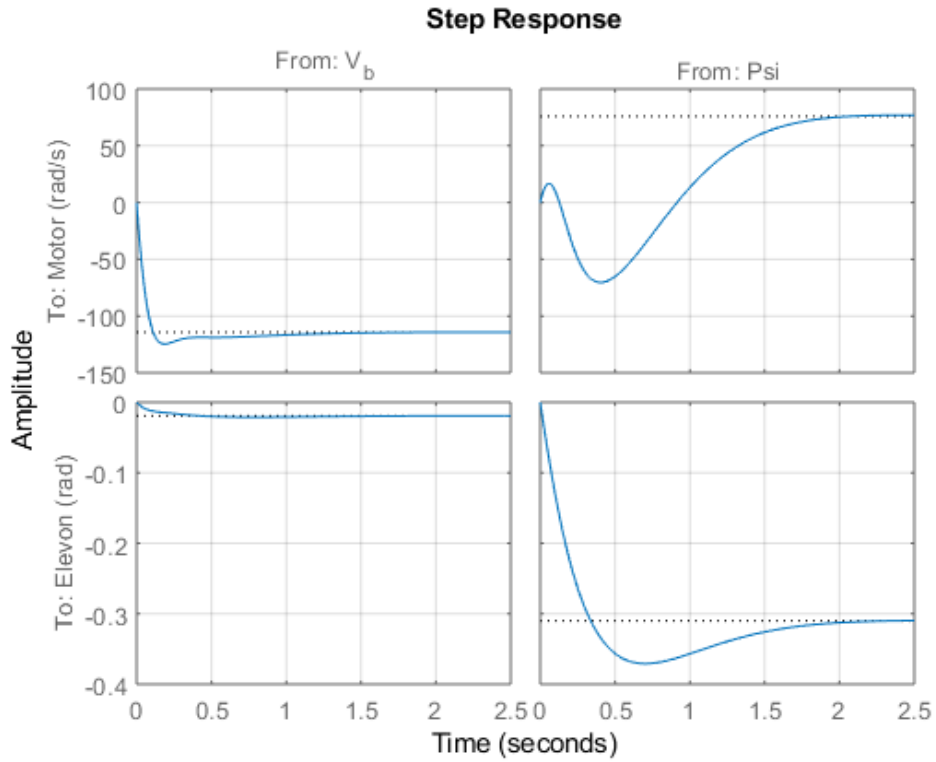


**Figure 13:** *Effect on actuators  $w$  and  $\delta$  to a step response*

Comparing this plot to the equilibrium values found at the beginning, it is possible to work out if these

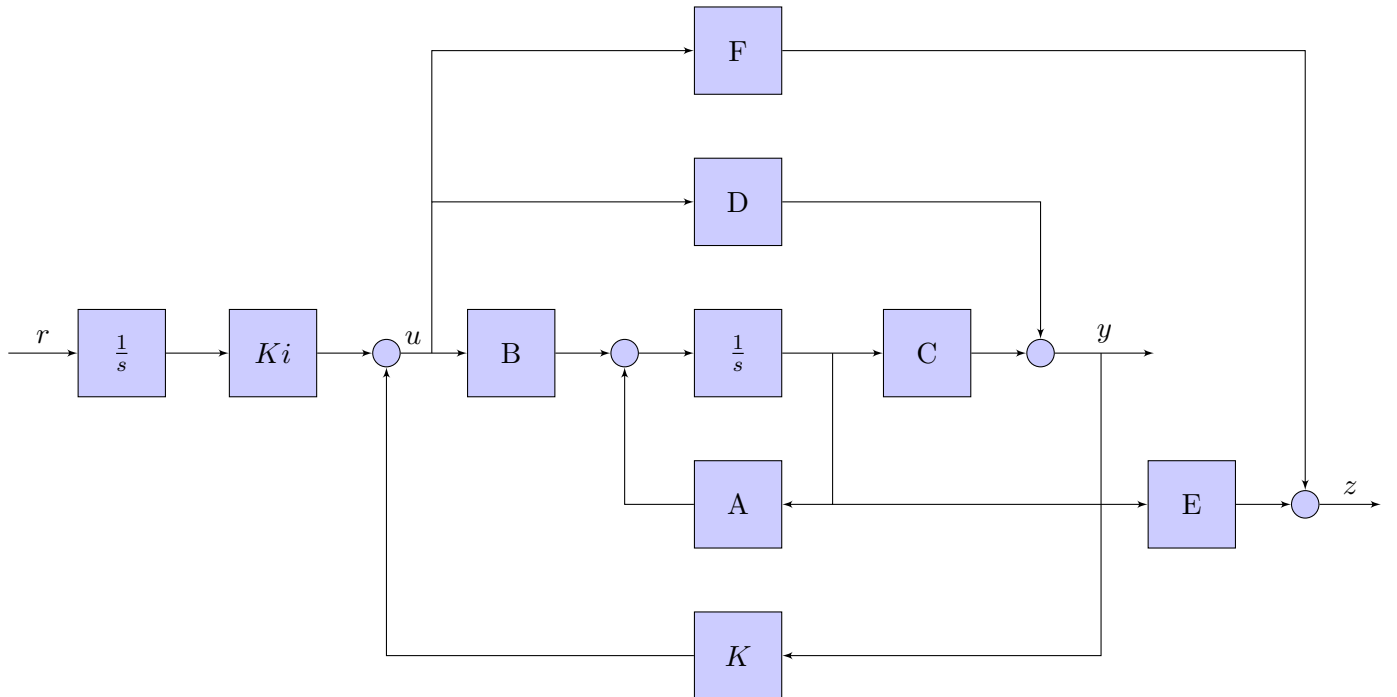
deviations from the equilibrium are feasible for the actuators. It was found that when the forward velocity is  $v_{ne} = 30m/s$ , the static angular velocity saturation for the engines is  $w_{sat} = 920.54rad/s$ . After analysing the actuator step response plot above, it was found that the peak response was  $-125rad/s$  and  $76.9rad/s$ . This would result in the maximum dynamic angular velocity being  $997.44rad/s$ . It is known that the motors being used on the MAVion are 1400kv with an 11.1V lithium polymer battery. This gives a theoretical maximum rating of 15,540RPM, or approximately  $1627rad/s$ . This provides evidence that the motors will be capable of successfully achieving the required manoeuvre. Similarly, the elevon deflection must be analysed to ensure this change in deflection will be possible. It is known that the maximum elevon deflection at the equilibrium point is  $-0.0381rad$ , which equates to approximately  $-2.18^\circ$ . From this equilibrium position, it can be seen that the elevon deflection should be approximately  $-0.37rad$ , or  $21.2^\circ$ . As this is less than  $27^\circ$ , the MAVion will be able to successfully alter the elevon deflection as required.

### Integrator Method:

In addition to the H matrix method, an integrator could instead be included to achieve a similar effect. Similar to the previous method, the following state space matrices will be used:

$$\begin{aligned}\dot{x} &= Ax + Bu \\ y &= Cx + Du \\ z &= Ex + Fu\end{aligned}\tag{25}$$

Similar to the H matrix method, this allows specific inputs to be controlled. In this case, the RC radio is still receiving commands from  $v_b$  (lateral velocity) and  $\dot{\psi}$  (yaw rate). Therefore, these should be the only outputs being controlled. The diagram below helps to depicts this method of integral action on the system.



As seen above, the control law is simply the error at the u output. This results in the following equation:

$$u = -Ky + K_i x_i\tag{26}$$

In order to add this integral action to the model, the number of states is increased to equal the number of inputs of the system, such that  $x_i \in \mathbb{R}^m$  is the integrator state matrix and  $K_i \in \mathbb{R}^{m \times m}$  is

the integrator gain matrix. From this, the following state, output and gain equations can be used:

$$\begin{aligned} x_a &= \begin{bmatrix} x \\ x_i \end{bmatrix} \\ y_a &= \begin{bmatrix} y \\ x_i \end{bmatrix} \\ K &= [K \quad -K_i] \end{aligned} \tag{27}$$

And to further expand equation 26, the equations above can be substituted in:

$$u = -[K \quad -K_i] \begin{bmatrix} y \\ x_i \end{bmatrix} \tag{28}$$

This can be further expanded after recalling that  $y = Cx + Du$ :

$$u = -[K \quad -K_i] \begin{bmatrix} Cx + Du \\ x_i \end{bmatrix} \tag{29}$$

This model can be further expanded to a common state space form by examining the diagram above. This provides the following equation which is clearly linked to the original state space equation  $\dot{x} = Ax + Bu$ :

$$\dot{x} = r - Ex - Fu \tag{30}$$

From this, it is then possible to generate the open loop state space model, where  $m = \text{inputs}$ ,  $n = \text{states}$  and  $p = \text{outputs}$ :

$$\begin{aligned} \dot{x} &= \begin{bmatrix} A & 0_{n \times m} \\ -E & 0_{m \times m} \end{bmatrix} x_a + \begin{bmatrix} B \\ -F \end{bmatrix} u + \begin{bmatrix} 0_{n \times m} \\ I_m \end{bmatrix} r \\ \dot{x} &= \begin{bmatrix} C & 0_{p \times m} \\ 0_{m \times n} & I_m \end{bmatrix} x_a + \begin{bmatrix} D \\ 0_{m \times m} \end{bmatrix} u + \begin{bmatrix} 0_{n \times m} \\ 0_{m \times m} \end{bmatrix} r \end{aligned} \tag{31}$$

And to then establish the closed loop state space model, the following control law can be developed from the equations above:

$$u = -(I + KD)^{-1}KCx + (I + KD)^{-1}K_ix_i \tag{32}$$

Allowing the final closed loop state space model to be found:

$$\begin{aligned} \dot{x} &= \begin{bmatrix} A - B(I + KD)^{-1}KC & B(I + KD)^{-1}K_i \\ -E + F(I + KD)^{-1}KC & -F(I + KD)^{-1}K_i \end{bmatrix} x_a + \begin{bmatrix} 0_{n \times m} \\ I_m \end{bmatrix} r \\ z &= [E - F(I + KD)^{-1}KC \quad F(I + KD)^{-1}K_i] x_a \end{aligned} \tag{33}$$

With the closed loop state space system now developed, it is possible to analyse the effect of including the integrator in the system. This is possible by analysing the effect of a step response on the system. It can be seen in the figure below that all plots either converge to 0 or 1, providing evidence that the integrator is working as expected. In addition to this, it can be seen that the settling time and peak response is of an acceptable nature for a small scale drone such as the MAVion.

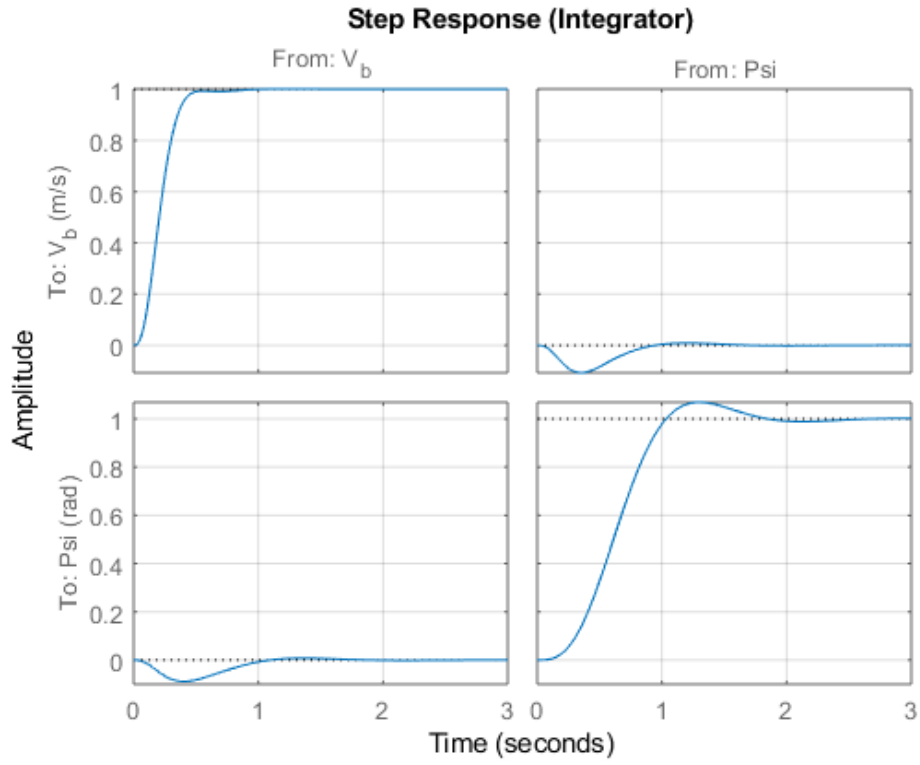


**Figure 14:** *Effect on  $v_b$  and  $\psi$  to a step response*

Along with this, it is also important to consider the saturation limits of the actuators ( $w$  and  $\delta$ ), as previously discussed. If these are not considered, it is possible that the tuned controller may not physically work on the model due to certain actuators reaching their maximum limits. The plot below shows the actuator movements when the forward velocity is set to  $v_{ne} = 30m/s$ .

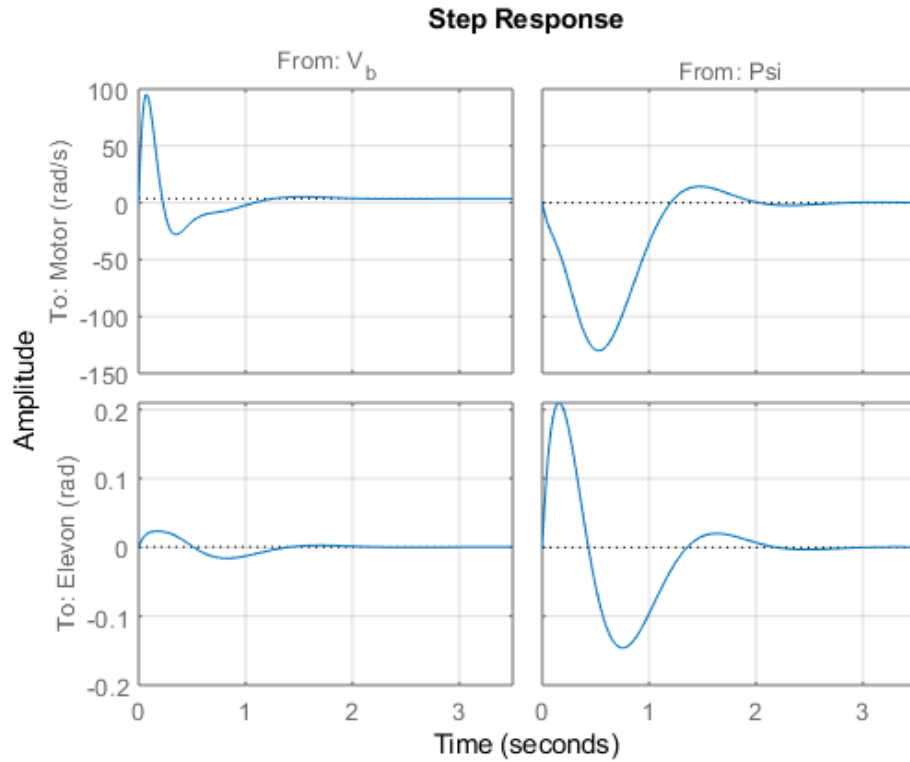


**Figure 15:** *Effect on actuators  $w$  and  $\delta$  to a step response*

Comparing this plot to the equilibrium values found at the beginning, it is possible to work out if these deviations from the equilibrium are feasible for the actuators. It was found that when the forward velocity is  $v_{ne} = 30m/s$ , the static angular velocity saturation for the engines is  $w_{sat} = 920.54rad/s$ . After analysing the actuator step response plot above, it was found that the peak response was  $94.9rad/s$  and  $-130rad/s$ . This would result in the maximum dynamic angular velocity being  $1015.44rad/s$ . As previously discussed, it is known that the motors being used on the MAVion are 1400kv with an 11.1V lithium polymer battery. This gives a theoretical maximum rating of 15,540RPM, or approximately  $1627rad/s$ . This provides evidence that the motors will be capable of successfully achieving the required manoeuvre. Similarly, the elevon deflection must be analysed to ensure this change in deflection will be possible. It is known that the maximum elevon deflection at the equilibrium point is  $-0.0381rad$ , which equates to approximately  $-2.18^\circ$ . From this equilibrium position, it can be seen that the elevon deflection should be approximately  $0.21rad$ , or  $12^\circ$ . As this is less than  $27^\circ$ , the MAVion will be able to successfully alter the elevon deflection as required.

#### **H Matrix vs. Integrator:**

Through the detailed analysis of both the H matrix and integrator method, it can be seen that both techniques appear to result in a similar outcome on the final system response. Although the outcome is the same, both methods work in very different ways, with the integrator method being more robust to physical errors in the system. In comparison to the H matrix method, the integral method allows for uncertainties in the plant model. This is a major advantage over the H matrix method and is the reason why the integral action is the chosen technique for the LQR controller.

## **5 Conclusion**

In the next few years, it is likely that the popularity and demand for convertible drones will continue to grow. This will be likely attributed to their favourable qualities such as reduced actuators, slim and transportable nature and reduced impact on the environment. Although it initially appeared as though the analysis of a convertible drone may be more complicated due to possible coupling of dynamics, it was found that both the longitudinal and lateral components of the MAVion could be independently and successfully analysed. After the analysis of these dynamics, a suitable controller was designed, with an LQR controller being chosen with integral action. This resulted in the MAVion having both fast response times, along with the actuator values being within the required limits.

## References

- [1] Scientist, Rocket. “The Different Types of Drones Explained.” Drone Omega, 9 Jan. 2018, [www.droneomega.com/types-of-drones/](http://www.droneomega.com/types-of-drones/).
- [2] “ATMOS UAV: VTOL Drones for Mapping amp; Surveying.” ATMOS UAV — VTOL Drones for Mapping amp; Surveying, [www.atmosuav.com/](http://www.atmosuav.com/).
- [3] “WingtraOne Surveying and Mapping Drone for High Accuracy over Large Areas.” Wingtra, [wingtra.com/mapping-drone-wingtraone/](http://wingtra.com/mapping-drone-wingtraone/).
- [4] “AeroVironment SkyTote.” AeroVironment SkyTote, 28 Jan. 2006, [www.designation-systems.net/dusrm/app4/skytote.html](http://www.designation-systems.net/dusrm/app4/skytote.html).
- [5] “Tailsitters vs. Quadplanes – Why a VTOL Tailsitter Is the Best Surveying Drone for Your Mapping Missions.” Wingtra, 30 Apr. 2019, [wingtra.com/tailsitters-vs-quadplanes-why-a-vtol-tailsitter-is-the-best-surveying-drone-for-your-mapping-missions/](http://wingtra.com/tailsitters-vs-quadplanes-why-a-vtol-tailsitter-is-the-best-surveying-drone-for-your-mapping-missions/).